JOURNAL OF GEOPHYSICAL RESEARCH, VOL. 115, D10213, doi:10.1029/2009JD012518, 2010

Attributes of mesoscale convective systems at the land-ocean transition in Senegal during NASA African Monsoon Multidisciplinary Analyses 2006

Marcia S. DeLonge,[1] Jose D. Fuentes,[1] Stephen Chan,[1] Paul A. Kucera,[2] Everette Joseph,[3] Amadou T. Gaye,[4] and Badiane Daouda[4]

Received 19 May 2009; revised 19 November 2009; accepted 28 December 2009; published 29 May 2010.

[1] In this study we investigate the development of a mesoscale convective system (MCS) as it moved from West Africa to the Atlantic Ocean on 31 August 2006. We document surface and atmospheric conditions preceding and following the MCS, particularly near the coast. These analyses are used to evaluate how thermodynamic and microphysical gradients influence storms as they move from continental to maritime environments. To achieve these goals, we employ observations from NASA African Monsoon Multidisciplinary Analyses (NAMMA) from the NASA S band polarimetric Doppler radar, a meteorological flux tower, upper-air soundings, and rain gauges. We show that the MCS maintained a convective leading edge and trailing stratiform region as it propagated from land to ocean. The initial strength and organization of the MCS were associated with favorable antecedent conditions in the continental lower atmosphere, including high specific humidity (18 g kg^{-1}), temperatures (300 K), and wind shear. While transitioning, the convective and stratiform regions became weaker and disorganized. Such storm changes were linked to less favorable thermodynamic, dynamic, and microphysical conditions over ocean. To address whether storms in different life-cycle phases exhibited similar features, a composite analysis of major NAMMA events was performed. This analysis revealed an even stronger shift to lower reflectivity values over ocean. These findings support the hypothesis that favorable thermodynamic conditions over the coast are a prerequisite to ensuring that MCSs do not dissipate at the continental-maritime transition, particularly due to strong gradients that can weaken West African storms moving from land to ocean.

Citation: DeLonge, M. S., J. D. Fuentes, S. Chan, P. A. Kucera, E. Joseph, A. T. Gaye, and B. Daouda (2010), Attributes of mesoscale convective systems at the land-ocean transition in Senegal during NASA African Monsoon Multidisciplinary Analyses 2006, *J. Geophys. Res.*, *115*, D10213, doi:10.1029/2009JD012518.

1. Introduction

[2] West African mesoscale convective systems (MCSs) are the dominant source of rainfall in the Sahel [i.e., *Houze*, 1977; *Lebel et al.*, 2003] and are also linked to tropical cyclogenesis over the eastern Atlantic Ocean [*Thorncroft and Hodges*, 2001]. MCSs strongly influence atmospheric energy transport, thereby modulating climate at regional and global scales. They can also significantly alter the vertical distribution of atmospheric trace gases (e.g., ozone [*Grant et al.*, 2008]) and aerosols [*Flamant et al.*, 2007]. Drought conditions in the Sahel in the 1970s and 1980s [*Nicholson*, 2000] brought much attention to the large interannual variability of MCSs. More recently, the debate over whether the frequency of tropical storm generation is increasing over the eastern Atlantic Ocean [*Goldenberg et al.*, 2001; *Webster et al.*, 2005; *Emanuel*, 2006; *Landsea*, 2007] has prompted even greater interest in MCSs. Of particular interest is the relationship of these storms to tropical cyclogenesis in the eastern Atlantic Ocean, as such tropical storms can make their way to Central America and North America [*Goldenberg et al.*, 2001].

[3] MCS propagate through sub-Saharan Africa during the summer rainy season [*Hamilton and Archbold*, 1945; *Eldridge*, 1957; *Carlson*, 1969]. Field research, based primarily on radar and rawinsonde information, has revealed considerable details about dynamic and thermodynamic characteristics of these MCSs, particularly over the eastern

[1]Department of Environmental Science, University of Virginia, Charlottesville, Virginia, USA.
[2]Research Applications Laboratory, National Center for Atmospheric Research, Boulder, Colorado, USA.
[3]Department of Physics and Astronomy, Howard University, Washington, D. C., USA.
[4]Laboratoire de Physique de l'Atmosphère et de l'Océan-Siméon Fongang, Ecole Supérieure Polytechnique, University Cheikh Anta Diop, Dakar, Senegal.

0148-0227/10/2009JD012518

Atlantic Ocean [e.g., *Zipser*, 1969; *Houze and Betts*, 1981; *Roux*, 1988]. Other studies have used satellite observations to examine their development and dissipation over land [*Laing and Fritsch*, 1993; *Hodges and Thorncroft*, 1997; *Mathon and Laurent*, 2001; *Gaye et al.*, 2005; *Laing et al.*, 2008]. Numerical models have also been used to better understand storm features [e.g., *Diongue et al.*, 2002]. Findings show that West African MCSs are most frequently organized as squall lines on the order of hundreds of kilometers long and a few tens of kilometers wide [*Houze*, 1977]. The storms are associated with African Easterly Waves (AEWs) [e.g., *Carlson*, 1969; *Frank*, 1970], which are known to originate as instabilities due to interactions between the African Easterly Jet (AEJ) and convection over the highland regions [*Berry and Thorncroft*, 2005]. MCSs ordinarily occur under conditions with a strong low-level wind shear, large amounts (>2500 J kg^{-1}) of convective available potential energy (CAPE), and a strong AEJ (at ~650 hPa) [*Parker et al.*, 2005]. The systems move westward at speeds of about 10–20 m s^{-1} for a total lifetime of about 25 h [*Laing et al.*, 2008]. During this lifetime, MCSs experience a series of cycles (including decay and regeneration) that typically last a few hours [*Leary and Houze*, 1979; *Trier et al.*, 1997; *Rasmussen and Rutledge*, 1992; *Frederick and Schumacher*, 2007].

[4] MCSs are commonly organized into two dominant regions, a narrow leading edge and an extensive trailing region, which are associated with distinct forms of rainfall: convective and stratiform [e.g., *Houze*, 1977, 2004; *Frederick and Schumacher*, 2007]. In the deep leading edge, strong convective updrafts lead to saturation and rapid formation of cloud droplets or ice crystals. As these hydrometeors grow (due to the Bergeron process, aggregation, riming, collision, and coalescence), they begin to fall rapidly (i.e., as rain, graupel). The result is a region of intense convective rainfall, with downdrafts that transport cooler, drier air from aloft to the surface. Behind this convective region, frozen hydrometeors grow primarily due to vapor deposition in a weaker mesoscale updraft, falling slowly to the melting layer, which is indicated by a bright band in the radar reflectivity field. Much stratiform rain evaporates in the lower dry regions of the storm, and what reaches the surface is comparatively light rainfall. The presence of these regions, whose microphysical differences allow them to be identified in vertical profiles of reflectivity, has important implications.

[5] Past studies showed that maritime and continental storms exhibit features that are spatially and temporally different [*Yuter and Houze*, 1995; *Zipser and Lutz*, 1994; *Schumacher and Houze*, 2003; *Zipser et al.*, 2006; *Futyan and Del Genio*, 2007; *Toracinta et al.*, 2002; *Cecil and Zipser*, 2002; *Nesbitt and Zipser*, 2003]. Overall, storms over the ocean produce more stratiform rain, exhibit smaller amplitudes in the diurnal cycles, have less ice content, and generate less lightning. Over the interior of Africa, where ground observations are more limited, studies using temporally averaged observations from the Tropical Rainfall Measurement Mission (TRMM) indicate that continental storms are deeper and more intense and exhibit clouds with less stratiform rainfall than Atlantic storms [*Schumacher and Houze*, 2006; *Fuentes et al.*, 2008]. The distinctions between continental and maritime storms are likely related to differences in surface-atmosphere exchange processes and aerosol content over these surfaces. For example, whereas continental regions exhibit strong diurnal variability in energy exchanges with maximum values in the afternoon, fluxes are less variable and reach lower peaks over the ocean. For instance, sensible and latent heat fluxes over West Africa (Nigeria) on a dry day ranged between 0 and 320 W m^{-2} and between 0 and 50 W m^{-2}, respectively; on a wet day, these fluxes peaked at 102 and 320 W m^{-2}, respectively [*Mauder et al.*, 2007]. Over the tropical oceans, latent heat fluxes reach maximum values of about 160 W m^{-2} [*Feng and Li*, 2006]. Over the eastern tropical Atlantic Ocean specifically, latent heat fluxes average 76 ± 32.2 W m^{-2} [*White et al.*, 1995]. In contrast, sensible heat fluxes over tropical oceans remain lower than 10 W m^{-2} [*da Silva et al.*, 1994; *White et al.*, 1995]. As with the thermodynamic distinctions, the sources and types of aerosols differ over West Africa and the Atlantic Ocean (i.e., from terrigenous-dominated materials to sea-salt aerosols). Dust aerosols [*Dunion and Valden*, 2004] can impact cloud dynamics by serving as cloud condensation nuclei (CCN) and ice nuclei [*Twohy et al.*, 2009]. Thus, in the presence of dust layers, MCSs can experience aerosol-cloud microphysics interactions that may invigorate convection [*Koren et al.*, 2005; *Khain et al.*, 2005], potentially offsetting the negative dust impacts in suppressing rainfall [*Rosenfeld et al.*, 2001; *Min et al.*, 2008; *Hui et al.*, 2008]. Therefore, a gradient in aerosol content may also contribute to differences in cloud microphysical properties observed over continental and maritime regions [*Rosenfeld*, 1999].

[6] Despite extensive knowledge about West African MCSs [e.g., see the review by *Houze* [2004]), thermodynamic, dynamic, and microphysical characteristics of their transition from the continental to the maritime environment remain poorly understood. The thermodynamic and microphysical gradients described above may help to explain why most MCSs dissipate as they approach the coast and move over the ocean, while only some strengthen and play a role in cyclogenesis [*Sall and Sauvageot*, 2005]. The influence of these gradients along the continental-to-ocean transect needs to be quantified to improve forecasts of tropical storm development and propagation [*Krishnamurti et al.*, 2007], as well as for the validation of satellite-based rainfall estimates.

[7] The objective of the present study is to investigate dynamic, thermodynamic, and microphysical attributes of a West African MCS as it transitioned from a continental to a maritime environment. To achieve this objective, we first analyze surface and boundary layer characteristics before, during, and after the system passed. These analyses are then used as a framework to discuss the importance of the relationships between local surface and boundary layer conditions and a propagating MCS. Radar observations are utilized to identify key attributes of the system, such as structure and organization, vertical profiles of reflectivity, and microphysical composition, as it moved from land to ocean. Finally, a composite analysis of the vertical profiles of reflectivity from the seven other propagating, spatially extensive, well-observed storms is used to evaluate how the selected MCS compares to other West African storms in this transitional region.

[8] The MCS that we describe here, which passed over the study site at 0805 universal time coordinated (UTC, equivalent to local standard time in this region) on 31 August 2006

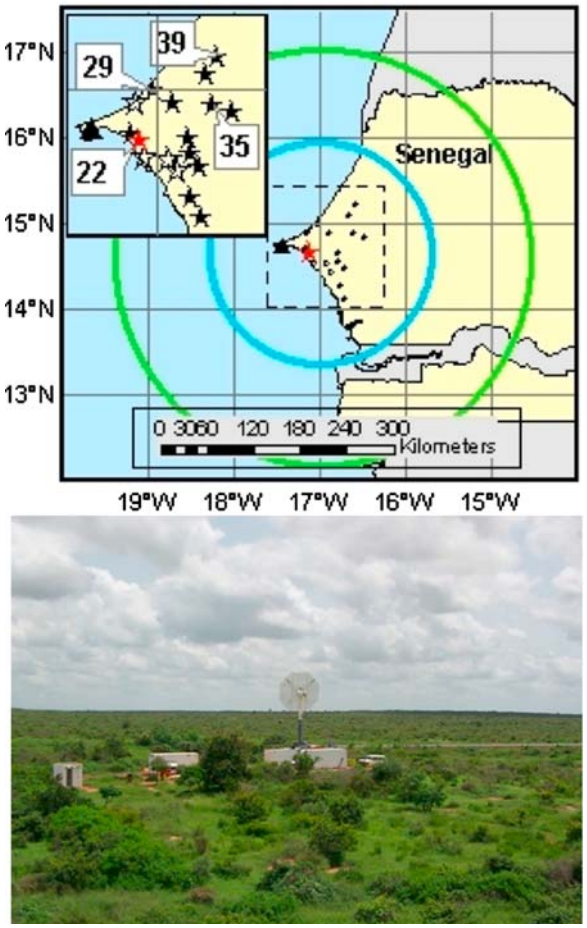

Figure 1. Location of study site (red star), Dakar (triangle), and rain gauges (stars). Circles show the radii of radar scans. The inner circle includes full-volume scans. (inset) The enlarged area denoted by the dashed square, identifying the gauges used in Figure 4. The photograph shows the radar and surrounding landscape.

(day of year 243), was 1 of 12 storms observed during the 2006 West African rainy season as part of the NASA African Monsoon Multidisciplinary Analyses (NAMMA). The system was a well-organized, fast-moving squall line with features such as a strong gust front, a bow-shaped convective leading edge, and an extensive trailing stratiform region. This paper presents the first observation-based analysis of the land-ocean evolution of a West African MCS sampled with colocated flux tower, upper air soundings, and a dual-polarized Doppler radar.

2. Methods

2.1. Site Characteristics

[9] The following analysis is based on observations made from a site located in Kawsara, Senegal (14.66°N, 17.10°W, 74 m above sea level; see Figure 1). The site is situated in a relatively flat landscape, making it amenable to studying surface-atmosphere exchanges of energy and momentum using eddy covariance methods. It is located approximately 10 km east of the Atlantic Ocean and 40 km southeast of Dakar, Senegal. This region is broadly known as the semi-arid Sahel savanna, and it falls in the center of a strong north-to-south rainfall gradient and on the cooler edge of an east-to-west temperature gradient [*Fall et al.*, 2006]. Around the site, the landscape consisted of patches of bare soil, grasses, and shrubs. The average and maximum height of the shrubs were 1.3 and 3.0 m, respectively. A village of 25 persons was located 200 m from the study site (Figure 1).

2.2. Radar Observations

[10] The NASA dual-polarized, S band Doppler (NPOL) radar provided continuous surveillance of precipitation during the NAMMA campaign. NPOL had a temporal scanning resolution of 15 min that included both long-range surveillance (0.8° tilt, 270 km) and full-volume (19 tilt levels, 150 km radius) scans, with a resolution of 1.4° (azimuth). The full-volume-scan included tilt angles from 0.7° to 33.0°, which in some cases was adjusted to 0.8° to 46.0° when storms were nearby the radar site. Radar reflectivity (z (mm^6 m^{-3})) and reflectivity factor (Z (db$Z$)), which provide an estimate of the intensity of the backscatter, were calculated as by *Rogers* [1979]. Radar volume scans were quality controlled by first removing data with invalid reflectivity values (>65 db$Z$). The data were subsequently filtered based on range-dependent threshold correlation coefficients (i.e., the correlation between the horizontal and vertical polarizations) [*Ryzhkov et al.*, 1994], radar reflectivity, and Doppler velocities. A comparison of radar reflectivity values observed by NPOL and the Precipitation Radar on the TRMM satellite showed a reflectivity bias of −2.0 dB, which was used to further correct radar observations. A second pass of filters was applied, which included evaluations of the vertical extent of echoes (based on *Steiner and Smith* [2002]), ground clutter (incorporating a method due to *Rinehart* [2004]), and backlobes. Finally, random noise was removed and the edges were smoothed using a neighborhood technique (i.e., through a comparison of point observations with nearby values).

[11] In addition to reflectivity, other derived radar variables included mean Doppler velocity (V_r (m s^{-1})), spectral width (SW (m s^{-1})), differential reflectivity (Z_{dr} (dB)), specific differential phase (K_{dp} (deg km^{-1})), differential phase (ψ_{dp} (deg)), and correlation between horizontal and vertical polarizations (ρ_{hv} (0–1)). *Bringi and Chandrasekar* [2001] provide detailed information about the polarimetric fields. Unfortunately, NPOL data are not reliable during the times when the antenna is wet (J. Gerlach, personal communication, NASA, 2009); therefore, the radar observations during these times were excluded from the analyses. Evaluations of the quality of NPOL observations during all other periods, when the antenna is not wet, indicate that the polarimetric fields tend to have larger uncertainties as compared to other polarimetric radar systems. However, the measurements fall within expected limitations, and the polarimetric fields provide useful information about cloud properties (data not shown).

[12] Using the radar observations described above, we can provide information about the precipitation characteristics such as the size, shape, density, and uniformity of the hydrometeors in a given radar echo. For this study, we determined the spatial distribution of hydrometeors within the 31 August MCS during the land-to-ocean transition, using the National Center for Atmospheric Research polarimetric

particle identification algorithm [*Vivekanandan et al.*, 1999]. The algorithm classifies radar echoes into 14 categories using a fuzzy logic methodology to determine the most probable dominant hydrometeor (e.g., rain, snow, hail, ice) in a given region of the cloud. For this analysis, the algorithm was initialized using a rawinsonde temperature profile obtained from the study site preceding the MCS passage. A horizontal resolution of 2 km and a vertical resolution of 1 km were used. Finally, rainwater content (W (g m^{-3})) of the system was estimated according to the parameterization from *Bringi and Chandrasekar* [2001],

$$W(Z_h, Z_{\mathrm{dr}}) = c_1 Z_h^{a_1} 10^{0.1 b_1 Z_{\mathrm{dr}}}. \quad (1)$$

Z_h is the corrected horizontal polarization reflectivity in units of mm^6 m^{-3}, Z_{dr} is the differential reflectivity in dB, and a_1, b_1, and c_1 are parameters specific to an S band radar (i.e., 0.89, −4.16, and 0.7×10^{-3}, respectively). Total rainwater content in each 1 km layer bin was calculated by multiplying each grid cell by its volume.

2.3. Rain Gauge Network

[13] A network of tipping bucket rain gauges (model 6011-A, Qualimetrics, Sacramento, CA, and model TB3, Hydrological Services, Sydney, Australia) was deployed in western Senegal to provide information on the spatial and temporal variability of rainfall. A large-scale (18 gauges) and a high-density (20 gauges) network were deployed during the start of the rainy season in June 2005 and August 2006, respectively. Rain gauges recorded the time when 0.254 mm of rainfall occurred. The resulting data were stored on data loggers (model HOBO U12, Onset Corporation, Bourne, MA) and were visited weekly for data collection. Data were quality controlled by removing spurious records (e.g., false tips) and flagging missing periods. In this study, 18 gauges (Figure 1) were used to investigate the frequency and regional variability of rainfall near the radar site. Of these, 13 gauges (Figure 1, stars) reported rainfall on 31 August 2006 and were used to determine the amount and variability of rainfall along the northeast-to-southwest transect of the storm.

2.4. Surface Observations

[14] Meteorological variables were measured on a 12 m guyed tower (Universal Manufacturing/Universal Tower, Clinton Township, MI). Air temperature at five levels above ground was measured using fan-ventilated platinum thermistors (model 41342, R.M. Young Company, Traverse City, MI). Relative humidity was measured at 1.5 m with a hygristor (model 41382, R.M. Young Company). Incoming and outgoing solar (K), and terrestrial (L) irradiance levels were measured at 8 m above ground (model CNR1, Kipp and Zonen, Delft, Netherlands). Using these irradiance measurements, the net radiation (R_{net}) at the site was estimated as

$$R_{\mathrm{net}} = K_{\mathrm{incoming}} - K_{\mathrm{outgoing}} + L_{\mathrm{incoming}} - L_{\mathrm{outgoing}}. \quad (2)$$

The L_{outgoing} includes terrestrial energy emitted by the surface and incoming atmospheric thermal energy reflected by the surface. To determine surface-atmosphere exchanges of energy, a three-dimensional sonic anemometer (model Sx, Applied Technology, Longmont, CO) and an infrared gas analyzer (model LI-7500, LI-COR, Lincoln, NE) were deployed on the tower at 5 m above ground. The resulting 10 Hz data were stored on a computer for subsequent analyses. Turbulent fluxes of sensible heat (H) and latent heat (LE) were calculated over 30 min periods using eddy covariance methods,

$$H = -\overline{\rho} C_p \overline{w' T'} \quad (3)$$

$$LE = -\overline{\rho} L_v \overline{w' q'}. \quad (4)$$

w is vertical velocity, q is specific humidity, T is air temperature, ρ is air density, C_p is the specific heat of dry air at constant pressure, and L_v is the latent heat of vaporization. Quantities in primes represent the deviation from the 30 min mean, and the overbar denotes the average quantities over 30 min periods. Using these turbulent fluxes, the Bowen ratio ($\beta = H/LE$) was calculated to determine the partitioning of available energy into sensible and latent heating. To obtain estimates of atmospheric turbulence, the friction velocity u^* was calculated according to (when the flow is aligned to the east-west component),

$$u^* = \sqrt{\overline{\mathbf{u}'\mathbf{w}'}}. \quad (5)$$

u represents the horizontal wind speed. To determine the surface energy balance, the soil heat flux G was determined using plates (model HFT3, Campbell Scientific, Logan, UT) buried at 2 cm below the soil surface. Two plates were placed in the soil to represent fluxes for surfaces occupied by grasses and shrubs, respectively. To account for the landscape heterogeneity, belowground measurements (soil temperature, moisture, and heat flux) were taken beneath both shrubs and grasses.

2.5. Tropospheric Observations

[15] Rawinsondes (RS92-SGP, Vaisala, Helsinki, Finland) were launched from the study site to investigate thermodynamic and dynamic states of the atmosphere preceding and following the MCS. Between 19 August and 16 September 2006, 72 sondes were launched. Sondes were held at 1.5 m for 5 min prior to launching to ensure the proper sensor conditioning. Measurements of air temperature, pressure, relative humidity, wind speed, and wind direction were recorded every 2 s during sonde ascent. Because past research showed a significant daytime dry bias in Vaisala RS92 sondes [*Vömel et al.*, 2007; *Yoneyama et al.* 2008], values in the lower troposphere were compared with humidity observations from the hygristor and the water vapor gas analyzer. In the lower atmosphere, humidity data sets did not exhibit biases, and therefore it was not necessary to correct the sounding humidity information.

[16] From the state variable measurements, specific humidity (q (g kg^{-1})), virtual potential temperature (θ_V (K)) (i.e., the temperature that dry air would require to possess the same density as a moist air parcel, which is then brought adiabatically to the surface), and equivalent potential temperature (θ_E (K)) (i.e., a thermodynamic quantity conserved in moist adiabatic processes) were calculated as outlined by *Betts et al.* [2002].

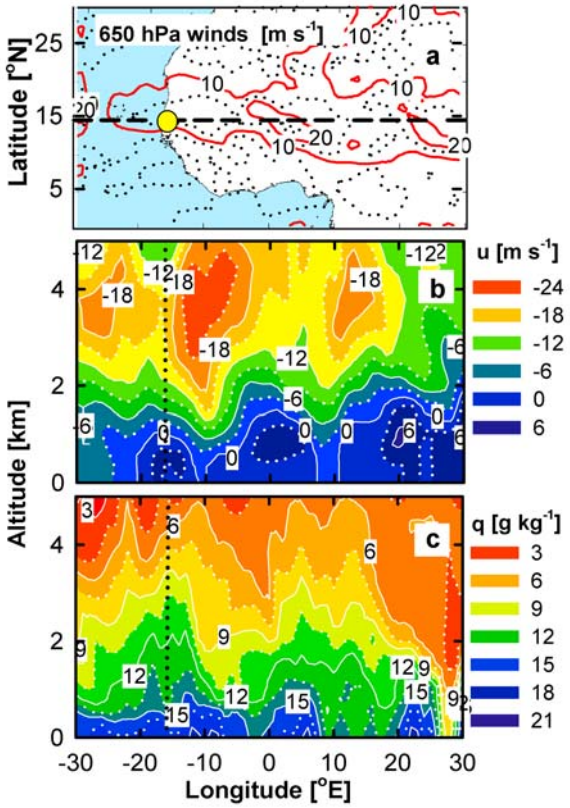

Figure 2. Synoptic overview at 0600 UTC on 31 August 2006. (a) Map showing zonal wind speed at 650 hPa. The study site in Senegal is shown by the dot, and the 15°N transect is shown by the dashed line. (b) Vertical cross section of east-west winds (u) (the contour lines show 5 m s^{-1} intervals). The site location is indicated by the dotted vertical line. (c) Vertical cross section of specific humidity (q) (the contour lines show 4 g kg^{-1} intervals).

[17] Convective available potential energy (CAPE (J kg^{-1})), a measure of the maximum energy available to convection due to parcel buoyancy, was calculated as

$$\mathrm{CAPE} = \int_{z_{\mathrm{LFC}}}^{z_{\mathrm{EL}}} g\left(\frac{T_{v\,\mathrm{parcel}} - T_{v\,\mathrm{envt}}}{T_{v\,\mathrm{envt}}}\right) dz. \tag{6}$$

T_v is the virtual temperature, z_{LFC} is the level of free convection (LFC), and z_{EL} is the equilibrium level. In addition, convective inhibition (CIN, (J kg^{-1})), the energy barrier that must be overcome by forced ascent to get an air parcel to the LFC, was calculated as

$$\mathrm{CIN} = \int_{z_0}^{z_{\mathrm{LFC}}} g\left(\frac{T_{v\,\mathrm{parcel}} - T_{v\,\mathrm{envt}}}{T_{v\,\mathrm{envt}}}\right) dz. \tag{7}$$

z_0 denotes the ground level.

2.6. Vertical Profiles of Radar Reflectivity

[18] Contoured frequency with altitude diagrams (CFADs) [*Yuter and Houze*, 1995] of reflectivity values were created to reveal statistical characteristics of the vertical structure of the MCS. For the CFADs, sections of the MCS were first classified into categories describing the underlying surface (e.g., land or ocean), as well as the system region (e.g., convective or stratiform). A land-ocean mask was created to define the surface type. A buffer area including 14 km (seven grid cells) to the east and west of the coastline was excluded from the analyses. This coastal area was excluded to emphasize differences between the land and the ocean (which would have been obscured by including the transition region). The convective-stratiform separation was completed using the methodology of *Steiner et al.* [1995]. The CFADs were based on the Cartesian−gridded data and were made at a vertical resolution of 1.5–2 km (1.5 km through 10 km) and with reflectivity bins of 2 db$Z$. To avoid biased results, CFADs only report observations at heights that represent at least 2% of the total data points [*Yuter and Houze*, 1995].

[19] CFADs were created for individual scans during the case study and also for the complete 31 August event. An additional composite CFAD is included to represent all other spatially extensive storms that propagated through the radar domain (in majority) during NAMMA. The composite CFADs were created to identify overall features of the vertical reflectivity profiles within continental convective, continental stratiform, maritime convective, and maritime stratiform regions. For both of the composites (for the 31 August and for all other events), the differences in the relative frequencies of reflectivity values in land versus ocean were also calculated (separately for stratiform versus convective areas). Finally, the mean reflectivity values at each vertical level were determined, and statistical t tests for two independent samples were performed (at each level) to evaluate the significance of the observed differences between the land and the ocean. This analysis is presented to highlight the differences between the land and ocean reflectivity profiles.

3. Results and Discussion

3.1. Synoptic Conditions

[20] The MCS in the case study originated to the northeast of the study site around 1400 UTC on 30 August 2006 in highland regions near Mali (inferred from AMMA Meteosat SEVERI products) (http://loaamma.univ-lille1.fr/AMMA). The MCS continued to develop and strengthen as it approached the coast during the overnight hours. To gain an understanding of the winds and thermodynamic conditions associated with the system as it approached the study site, we present an overview of synoptic conditions at 0600 UTC using National Center for Environmental Prediction (NCEP) global tropospheric reanalyses (1° × 1°, 6 h product, ds083.2 [*Kalnay et al.*, 1996]) (http://dss.ucar.edu). Vertical cross sections from 30°W to 30°E at 15°N were created using reanalysis data from 19 pressure levels (from 1000 to 200 hPa). Winds at 650 hPa at 0600 UTC, when the system was 150 km northeast of the study site, show a strong AEJ (reaching 20 m s^{-1}) centered at latitude 15°N (Figure 2a). The vertical cross section of the east-west wind component (Figure 2b) along 15°N revealed winds with a strong easterly component (>20 m s^{-1}) throughout the upper troposphere, as well as surface flow (<1 km) with a weak westerly component (<5 m s^{-1}).

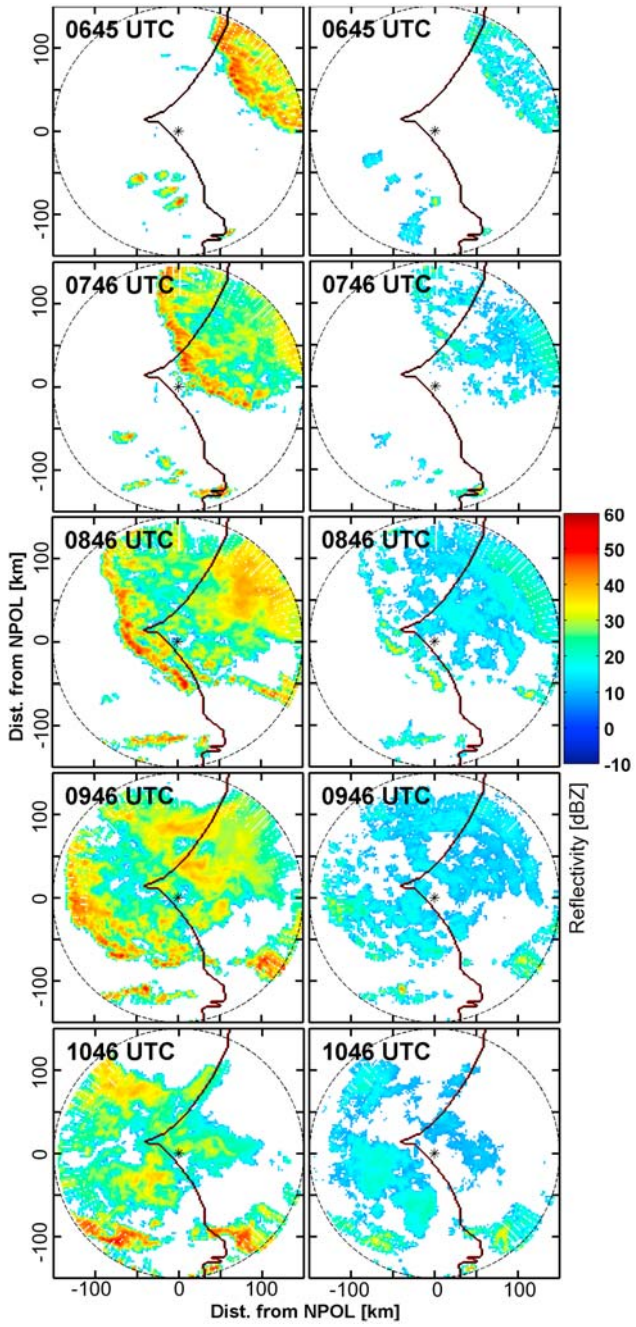

Figure 3. Radar cross sections ($r = 150$ km) showing hourly reflectivity values (in dBZ) from the NASA dual-polarized, S band Doppler (NPOL) radar from 0645 to 1045 UTC on 31 August 2006. Cross sections at (left) 3 km and (right) and 6 km. The coastline is shown in black.

[21] The NCEP moisture data at the coast at 0600 UTC were first contrasted with tower and radiosonde data from the study site and then evaluated to estimate the moisture content of the lower troposphere along the land-to-ocean transect. A vertical cross section of specific humidity from NCEP (also at 15°N) reveals gradients of moisture across the continental-to-maritime transect (Figure 2c). Peak levels of specific humidity were found at and near the coast prior to the MCS. This peak was pronounced in the continental range of the radar, with a specific humidity of 12 g kg^{-1} extending as high as 2 km from 12°W to 18°W (consistent with radiosonde observations at the study site). In contrast, west of 20°W (i.e., beyond the transition region) moist air only reached these specific humidity levels closer to the surface (<1 km). Peak moisture levels near the coast were likely due to both onshore flows and a continental convective boundary layer, which allowed moisture from the ocean to be mixed upwards into the troposphere.

3.2. Mesoscale Convective System Propagation and Spatial Extent

[22] The 31 August 2006 MCS was observed by NPOL between about 0600 and 1400 UTC, sampling the system formation, spatial extent, propagating speed, and other attributes as it transitioned from a continental to a maritime environment (Figure 3 shows hourly cross sections from 0645 to 1045 UTC). The system was first observed by the long-range surveillance scans as an organized squall line approaching from the northeast (250 km from the radar site) with a long (~260 km), bow-shaped leading edge. By 0600 UTC, the MCS was just entering the 150 km range of NPOL, moving at ~13 m s^{-1} and with maximum reflectivity values exceeding 45 db*Z*. As the squall line approached the study site (from 0600 through 0745 UTC), it propagated more quickly (18 m s^{-1}), the leading edge widened, reflectivity values remained intense (exceeding 50 db*Z*), and an extensive stratiform region became visible. This MCS likely sustained itself, maintaining its intensity, through strong updrafts and rapid diabatic heating associated with changes in the phase of water vapor. Shortly before the system reached the radar site, the mature convective squall line remained less than 50 km wide, whereas the stratiform region extended more than 200 km behind the storm leading edge.

[23] The northernmost edge of the squall line reached the coast at 0630 UTC, about 90 min before the system reached the study site (at 0805 UTC). The convective squall line maintained its organization and leading edge as it moved southwest, although the leading edge began to break away from the stratiform region, most notably after reaching the coast (~0845 UTC; see Figure 3). As the squall moved further southeastward over the Atlantic Ocean (~0945–1045 UTC), the system weakened and became less organized. By 1300 UTC the stratiform region had passed over the study site, moving mostly out of radar range by 1530 UTC.

3.3. Temporal and Spatial Variability of Rainfall

[24] To provide a spatial and temporal context of the 31 August MCS, we present both accumulated rainfall and average diurnal rainfall patterns observed by the rain gauges during NAMMA (Figure 4). The regional accumulated rainfall (average of 17 sites) showed the high frequency of large rain events (19) during the field season (Figure 4a). There were also several extended periods (>2 days) with no rainfall. Observations of rainfall over this domain were variable, as demonstrated by error bars in Figures 4a–4c.

[25] The majority of rain observed during August and September 2006 fell during the afternoon (1600–1900 UTC) (Figure 4b), particularly at the radar site. This afternoon maximum rainfall agrees with the climatology of continental MCSs, which have a well-defined diurnal pattern and most

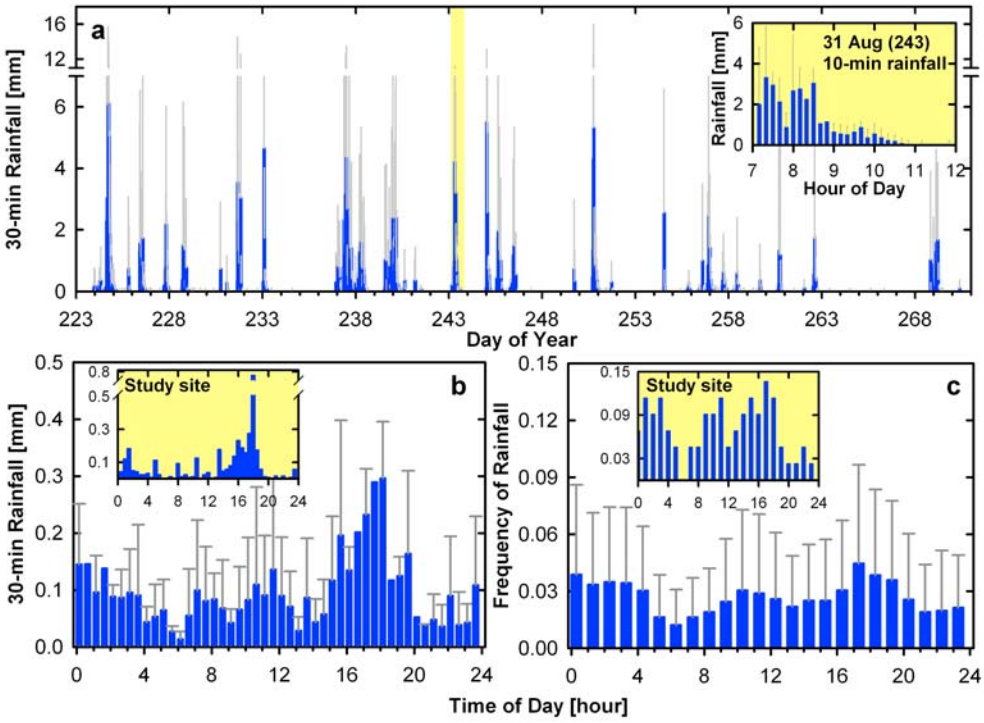

Figure 4. Spatial and temporal variability of NASA African Monsoon Multidisciplinary Analyses (NAMMA) 2006 (18 August to 27 September) rainfall. (a) Regional 30 min accumulated rainfall; gray bars show the standard deviation among 17 sites; (inset) regional 10 min accumulated rainfall during 31 August mesoscale convective system (MCS) (13 sites). (b) Regional 30 min diurnal rainfall; (inset) 30 min diurnal rainfall at study site. (c) Regional hourly frequency of rainfall; (inset) hourly frequency of rainfall at study site.

rain in the evening (1800–2400 UTC) [*Nesbitt and Zipser*, 2003]. During afternoon hours, heat and moisture content in the convective boundary layer at the study site regularly reached 20 g kg^{-1} (data not shown), providing a moisture source to passing storms. Not all of the rainfall pattern observed at the site, however, can be explained by diurnal variability. At the study site, a secondary weak maximum rainfall was observed during 0000–0400 UTC (Figure 4b, inset). Such maxima have been previously found in areas where rainfall is predominantly from storms that travel far from their point of origin [e.g., *Laing et al.*, 2008; *Negri et al.*, 1994]. In addition, the location of this study site, near the ocean, can favor the growth of slow or nonpropagating MCSs that are associated with AEWs and influenced by local moisture fluxes [*Laing et al.*, 2008]. In contrast to accumulated rain amounts, the relative frequency of rainfall events did not exhibit strong diurnal trends (Figure 4c), suggesting that rainfall amounts (in Figure 4b) can be indicative of storm size. Overall, large-scale dynamics rather than the diurnal cycle likely exerted the greater influence on the MCSs [*Sall and Sauvageot*, 2005; *Diedhiou et al.*, 2001].

[26] On the 31 August, rainfall was observed at the northeasternmost rain gauge sites beginning at 0700 UTC (Figure 4a, inset). Accumulated surface rainfall across the region (13 gauges) was spatially variable, although the three highest reports of total rainfall (25–35 mm, falling at intensities that at one point exceeded 90 mm hr^{-1}) were from the northeasternmost gauges. Total accumulated rainfall from four gauges is shown in Figure 5. These sites were selected specifically because they fell on northeast-to-southwest transects along the path of the propagating storm. Thus, gauges 35 and 22 measured rainfall from the center of the MCS, whereas 39 and 29 were at the northern edge; gauges 29 and 22 sampled rainfall at coastal, versus inland, locations. Although these measurements are insufficient to draw conclusions related to changes in the MCS, patterns of surface rainfall variability can be related to changes in thermodynamic and dynamic conditions throughout the radar domain.

[27] At the study site (22 in Figures 1 and 5), surface rainfall was among the lowest recorded, totaling 6.2 mm, with most of the accumulation occurring during the first 20 min (Figure 5). In the first few minutes, rain fell at a rate of 45 mm hr^{-1} before decreasing for the remaining minutes (data not shown). However, most of the rainfall fell at rates greater than 10 mm hr^{1}, indicating that rainfall was predominantly convective rather than stratiform [*Nzeukou and Sauvageot*, 2002]. The radar data, on the other hand, exhibited stratiform rainfall features (Figure 3). This discrepancy is due in part to the breakup of the stratiform region at around 0845 UTC. The lack of surface stratiform rainfall at the site was also likely related to the low-level (i.e., from the surface to the melting layer) evaporation of raindrops as they traveled from the clouds through relatively drier atmospheric layers in the rear of

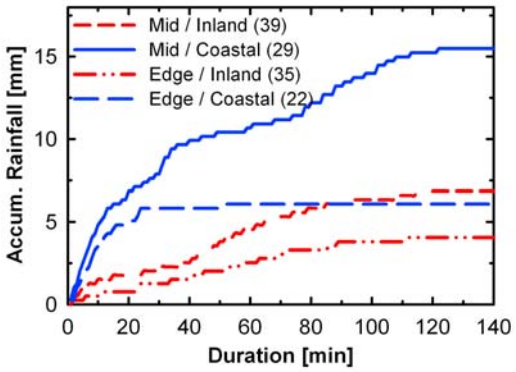

Figure 5. Spatial variability of rainfall during the 31 August 2006 MCS. Accumulated rainfall at four gauges (22, 29, 35, and 29; see Figure 1) that received rainfall from different regions of the storm.

the system (based on sonde profiles discussed below). Low-level evaporation signature for stratiform rainfall is a common occurrence over continental West Africa [*Hirose and Nakamura*, 2004; *Geerts and Dejene*, 2005; *Fuentes et al.*, 2008].

3.4. Prevailing Meteorological Conditions and Surface-Atmosphere Energy Exchange

[28] In order to understand how boundary layer processes can influence a propagating storm in this region, we discuss the antecedent surface-atmosphere energy exchanges and meteorological conditions. Solar irradiance and air temperature, wind speed and friction velocity, and surface energy fluxes observed for 1 day prior to (30 August) and 1 day following (1 September) the storm are reported (Figure 6). On the day prior to storm passage (30 August), maximum solar energy fluxes and air temperature reached 1000 W m^{-2} and 32°C, respectively. Such conditions promoted unstable atmospheric conditions and effective vertical transport of energy and water vapor, giving maximum daytime latent and sensible heat fluxes of 300 and 150 W m^{-2}, respectively. The available energy was portioned into latent heat in greater amounts than in sensible heating due to the moist surface conditions, with a daytime average $\beta = 0.6 \pm 0.1$. Atmospheric turbulence levels were moderate, with maximum wind speed and friction velocity of 4–5 and 0.5 m s^{-1}, respectively (Figure 6b). These conditions were similar to those observed at other West African sites [*Bagayoko et al.*, 2007; *Mauder et al.*, 2007] during the rainy season. Sufficient daytime latent and sensible heating, antecedent to storms, enhanced convection and thus strengthened storms as they propagated. High levels of energy transport on the day prior to the MCS were sufficient to create a favorable environment in the lower troposphere to prolong the life cycle of the storm.

[29] Sufficient thermodynamic instability existed in the atmosphere to fuel the early-morning MCS, despite the limited contribution of local surface-atmosphere energy exchanges. Since the system reached the study site only 1 h after local sunrise on 31 August, fluxes immediately prior to MCS passage were small (approximately zero) for both sensible and latent heat (Figure 6c). While the system was over the study site, net radiation increased at a low rate in response to prevailing overcast cloudy conditions. As the MCS moved away from the site, the available energy was partitioned to favor latent heating even more greatly (with a daytime average $\beta = 0.4 \pm 0.1$). The higher partitioning to latent heating can be explained by the increased soil moisture (11%–14%) due to rainfall. Sensible heat fluxes, on the other hand, were suppressed immediately following the MCS due to the effect of storm evaporative cooling, which created nearly isothermal conditions (in contrast with typically unstable conditions) in the lower troposphere.

3.5. Thermodynamic Conditions and Boundary Layer Processes

[30] While the surface energy fluxes are critical drivers of how favorable an environment can become for storm development, thermodynamic conditions of the boundary layer indicate how readily available energy and moisture are transported to the cloud layer. Before the MCS, prior to sunrise (0500 UTC), the lower atmosphere over the study site was warm (305 K up to 0.5 km) and moist (20 g kg^{-1} up to 0.5 km) (Figure 7). These conditions prevailed due to weak (<5 m s^{-1}) northwesterly onshore flow. Morning soundings revealed substantial CAPE (3532 J kg^{-1}), from the high moisture and temperature levels, which supplied energy for the propagation of the passing system. In addition, the CIN was −1 J kg^{-1}, such that minimal inhibition to convection existed. Upper air soundings from Cape Verde, although distant from the coastal region and also likely

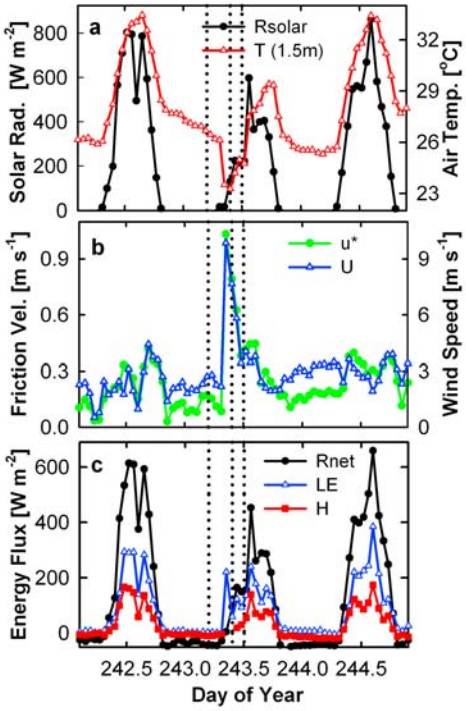

Figure 6. Surface conditions at the study site preceding and following the MCS; times of sondes in Figure 7 are shown by dotted lines. (a) Solar radiation (R_{solar}) and air temperature at 1.5 m (T), (b) friction velocity (u^*) and wind speed (U), and (c) fluxes of net radiation (R_{net}), latent heat (LE), and sensible heat (H).

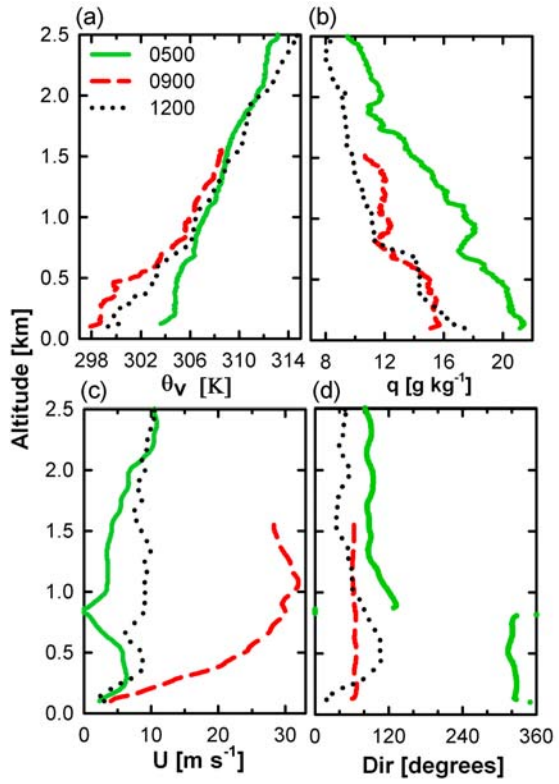

Figure 7. Thermodynamics and dynamics of the lower troposphere (0–2.5 km) before (0500 UTC), during (0900 UTC), and following the MCS (1200 UTC): (a) virtual potential temperature, (b) specific humidity, (c) wind speed, and (d) wind direction.

influenced by land, can likely provide indications of what conditions west of the coast were like on the morning of the storm. These soundings revealed a comparatively unfavorable lower troposphere, with a total CAPE of only 957 J kg^{-1} and CIN of −55 J kg^{-1} (not shown). Although they are not ideal indicators of antecedent conditions over the adjacent ocean, these measurements do show that less energy and more inhibition west of the coast may have contributed to MCS weakening. Some of this difference can be explained by the European Centre for Medium-Range Weather Forecasts analysis of sea surface temperatures (SSTs) and total column water (http://data-portal.ecmwf.int/data/d/interim_daily/). These analyses show that the ocean adjacent to the study site had SSTs over 28°C at 0600 UTC on 31 August 2006, whereas the temperature of the sea surface surrounding the Cape Verde islands only reached 26°C to 28°C. Similarly, total column water at 0000 UTC on 31 August exceeded 54 kg m^{-2} to the east of the study site, fell to between 48 and 54 kg m^{-2} over the study site, and was below 48 kg m^{-2} over Cape Verde.

[31] Changes in the lower troposphere at the study site indicate that available energy and moisture were vigorously transported upwards by updrafts (as previously shown by *Zipser* [1969]; see *Grant et al.* [2008] for more details of this case). Convective downdrafts associated with the MCS also transported cooler and drier air to the surface, as inferred from the strong drop in both moisture content and temperature in the lower atmosphere (to 298 K and 15 g kg^{-1}, respectively) (Figure 8). After the MCS passage (1200 UTC), an isothermal and drier lower atmosphere (up to 2.5 km) prevailed in response to the subsidence of air masses with lower heat and water vapor content. Such conditions lasted for less than 1 day, as the lower atmosphere became moister and warmer within 1 day after the system passed. Maximum zonal wind velocities of 20 m s^{-1} at about 4 km above the surface were observed during the time the gust front passed the study site (Figure 8). In the wake of the MCS, there was a strong wind shear (Figure 7c) in the lowest 4 km of the atmosphere. This shear was not observed prior to the MCS event, and thus was more likely a consequence of the storm. Such wind shear is commonly found in the rear inflow jet of MCSs [*Smull and Houze*, 1987; *Rasmussen and Rutledge*, 1992] and has been shown to be a dynamical response to heating in the convective leading edge [*Pandya and Durran*, 1996].

3.6. MCS Characteristics at the Continental-Maritime Transition

[32] One of the objectives of this study is to quantify the attributes of an MCS as it traveled from continental to oceanic environments. We begin our analysis by looking at the profiles of reflectivity in individual radar volume scans (of 15 min intervals) before discussing the composites. At 0645 UTC, while the leading edge was over land, the

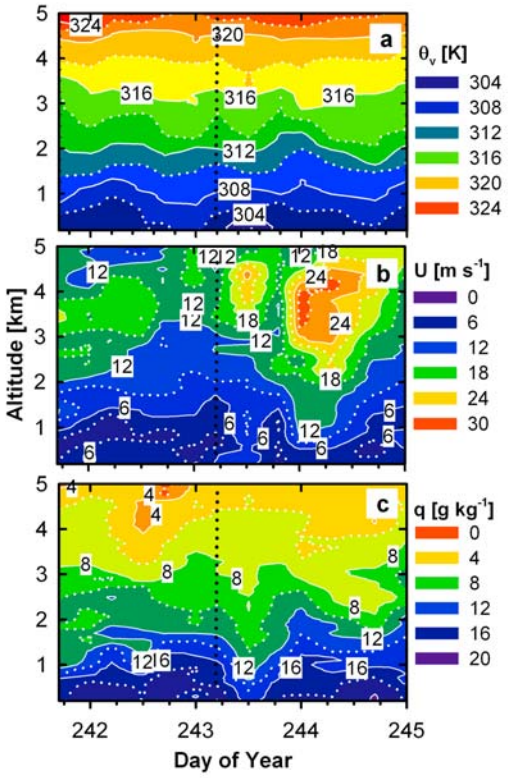

Figure 8. Lower tropospheric conditions at the study site preceding and following MCS passage (dotted line): (a) virtual potential temperature, (b) wind speed, and (c) specific humidity.

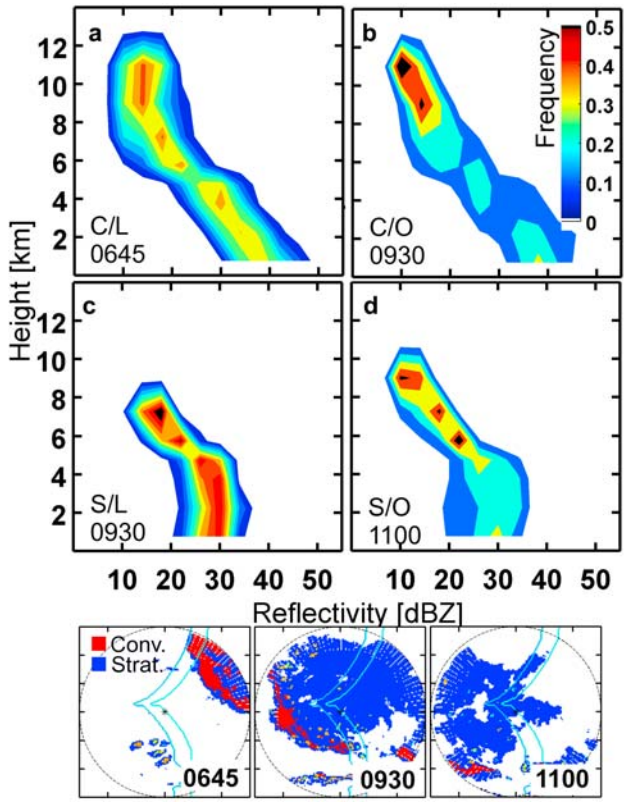

Figure 9. (top) Contoured frequency by altitude diagrams (CFADs) of reflectivity showing features of the 31 August 2006 MCS observed during individual volume scans in (a) the convective (C) region over land (L) at 0645 UTC, (b) the convective region over ocean (O) at 0930 UTC, (c) the stratiform (S) region over land at 0930, and (d) the stratiform region over ocean at 1100 UTC. (bottom) The cross sections show the areas of the storm that were classified as convective (red) versus stratiform (blue) at these times. The area east of the blue coast lines was classified as land and that to the west was classified as ocean, and the coastal region between the lines was excluded from CFAD analyses.

convective region of the system was intense, as indicated by reflectivity values reaching 50 db*Z* near the surface. The reflectivity values steadily decreased to about 20 db*Z* at 6 km above ground and extended vertically beyond 10 km (Figures 3 and 9a). By 0930 UTC, the full extent of the leading edge had reached the ocean, and the northern portion had been over the ocean for over 2 h. Over the ocean at 0930 UTC, the convective region exhibited similar reflectivity patterns as observed over land at 0645 UTC but with a smaller fraction of the convection reaching or exceeding peak values (e.g., 40 db*Z* in the lowest 2 km) (Figure 9b). In this case, the reduction of the frequencies (from land to ocean) of the highest reflectivities demonstrates a loss of intensity as the MCS transitioned. The more extensive stratiform region of the system had a well-defined bright-band feature in both the land (0930 UTC; see Figure 9c) and the ocean (1100 UTC; see Figure 9d) CFAD. Maximum reflectivity values (of over 30 db*Z*) in this region were found at over 4 km above ground, demarcating the location of the melting layer near the 0°C line. Over both land and ocean, maximum stratiform reflectivity values at and below the bright band were on the order of 10 db*Z* less than in the strongly convective leading edge. Such differences are expected, as the trailing stratiform region is known to be less intense, have smaller and fewer raindrops, and have lower reflectivity values near the surface. The CFADs of the stratiform region became more variable over ocean, as the frequency of lower reflectivity values increased at the expense of higher reflectivity values (e.g., indicating decreasing intensity). While it can be instructive to analyze individual volume scans, these observations alone reveal only snapshots of the MCS. In addition, the analysis is confounded due to the large difference (nearly 3 h) in the times that northern and southern ends of the squall line reached the coast. For example, while the 0645 UTC observations represented only areas of the storm influenced by a continental environment, the 0930 UTC observations included regions that had been over the ocean for variable amounts of time (0.5–3 h). Due to the limitations imposed by analyzing individual scans only, as well as the issue of spatially variable radar resolution, we turn our attention to the composite analysis.

[33] A composite analysis of the entire 31 August event provides a more robust and complete analysis of the reflectivity features over convective continental, convective oceanic, stratiform continental, and stratiform oceanic regions (Figures 10a–10d). For this analysis, land-ocean differences in the relative frequencies of reflectivity values are also presented (Figures 10e and 10f). In Figure 10, cool shades (blue) represent a decrease in the frequency of specific reflectivity values, whereas warm shades (red and yellow) identify an increase. In the overall analysis, Figure 10 reveals a shift toward lower reflectivity values in the convective region, especially in the lowest 4 km, indicating weaker convective cells with smaller and fewer raindrops reaching the surface. Lower intensities were also notable in the stratiform area, particularly in and around the melting layer. These changes were likely in response to less particle growth in weaker convective updrafts.

[34] Although the reflectivity profiles provide insights to MCS structure and evolution, additional radar analysis can reveal greater detail on the system's microphysical features as it moved from land to ocean (Figure 11). As the MCS approached from the northeast, a narrow region of heavy rainfall with large raindrops was identified in the lowest 4 km, below a growing area of deep convection. The presence of these hydrometeors was indicative of a strong convective updraft and downdraft associated with the squall line. A wider region (~20 km) with medium rainfall rates developed immediately behind the storm, followed by light rainfall (and ultimately drizzle) in the shallower stratiform region. Lighter rainfall is consistent with the presence of a mesoscale updraft and downdraft in the trailing region of the storm. The snow observed above the melting layer likely increased in a weak updraft before falling slowly below the melting later as medium-light rainfall. By the time the MCS reached the study site (Figure 11, at 0745 UTC), it had grown in vertical extent but exhibited less intense rainfall in the leading edge. As the system moved over the ocean and became less organized, regions of heavy rainfall in the leading edge continued to become narrower and weaker,

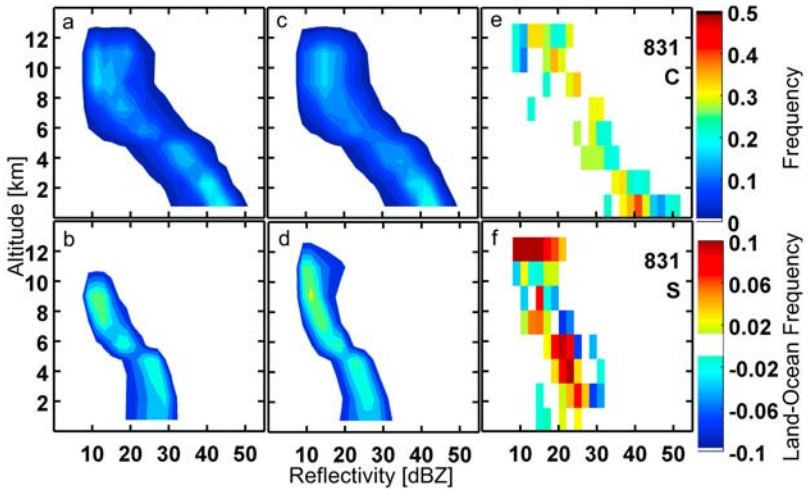

Figure 10. CFADs of reflectivity showing overall features of the 31 August 2006 MCS in the (a) convective (C) region over land (L), (b) stratiform (S) region over land, (c) convective region over ocean (O), and (d) stratiform region over ocean. These composites include all observations except scans influenced by the wet antenna. The differences in relative frequencies from land to ocean are shown in (e) convective and (f) stratiform regions (Difference = Ocean − Land; i.e., negative value/blue represents a decrease in relative frequency in ocean versus land). Note that absolute differences in frequencies <0.02 are not shown and all absolute frequency differences >0.1 are shown in red/blue.

whereas the stratiform region of light-medium rainfall remained strong and deep. While a thick layer of frozen precipitation formed over the coast by 0845 UTC (likely ice ejected from the strong updraft in the convective leading edge), only a thin layer extended over the ocean as the system propagated (e.g., even by 1045 UTC). Although many of the discussed changes likely resulted due to the life-cycle progression of the MCS, they were consistent with past observations showing that maritime storms can be more stratiform [*Geerts and Dejene*, 2005] and have lower ice content [*Zipser et al.*, 2006].

[35] Another objective of this study is to estimate the precipitable water from the 31 August MCS (Figure 12). As the MCS moved into the radar range of the full volume scans, the total observed rainwater content increased until 0945 UTC. The best estimates of the actual total system rainwater content can be made at 0945 UTC, when the majority of this extensive MCS was within the radar full-volume scans. At this time, radar observations of the storm covered a maximum area of 35,000 km^2 (of the 70,648 km^2 radar domain). The calculated rainwater content was less than 1 g m^{-3} in the majority of the domain (equivalent to 4×10^6 kg per 4 km^3 grid cell), and less than 4% of the observations reached 2–16 g m^3. The total integrated mass of water at this time was 2.6×10^{10} kg (an average of 0.74 mm over the area of the storm). Although the leading edge did remain within the full-volume scan at 1015 UTC, the total rainwater content actually decreased from 0945 to 1015 UTC. This finding again suggests that the MCS was weakening over the ocean. The high values of water content from 3 to 5 km, evident at all times, were most likely exaggerated due to the presence of the bright band.

[36] The analysis described above focused on a single MCS, providing evidence that a well-organized, extensive system can exhibit changes over the land-to-ocean transition. Furthermore, the nature of these changes is indicative of the presence of critical interactions between the system and local continental-maritime gradients. Because the results of a case study are limited, the prevailing vertical storm attributes during other NAMMA systems are shown in Figure 13. The overall composite CFADs reveal the statistical characteristics of reflectivity profiles from seven other extensive storms that were at different phases in their life cycles when they transitioned from land to ocean. The radar observations included are as follows: (1) 2045 UTC 27 August to 0716 UTC 28 August, (2) 1045–1730 UTC 29 August, (3) 2230 UTC 1 September to 0800 UTC 2 September, (4) 1230–2230 UTC 2 September, (5) 1515 UTC 7 September to 0700 UTC 8 September, (6) 0815–1630 UTC 11 September, and (7) 1930 UTC 13 September to 0815 UTC 14 September 2006. From this analysis, it is apparent that features observed in the 31 August MCS were also evident in other cases. As in the 31 August case, convective regions exhibited high surface reflectivity values (~40 db*Z*), with radar echo intensities decreasing with altitude to an altitude greater than 10 km. In stratiform regions, a distinctly different vertical reflectivity profile was observed with a clear, bright band signifying a melting layer near 4 km. In both the convective and stratiform regions, a slight shift from higher to lower reflectivity values throughout most of the reflectivity profile indicated that the intensity of the continental convection was slightly greater than neighboring maritime convection. Figure 14 shows the amount and significance of the difference between mean reflectivity values over the land and ocean at all vertical levels. The observed decrease in intensity (by an average of 1–3 dBZ) throughout the majority of both convective and stratiform profiles was significant at all levels ($p < 0.05$). In fact, the overall composite analysis revealed larger decreases in the average reflectivities (from land to ocean) than in the 31 August case. However, in both cases, the decreases in the regions that typically exhibit the highest

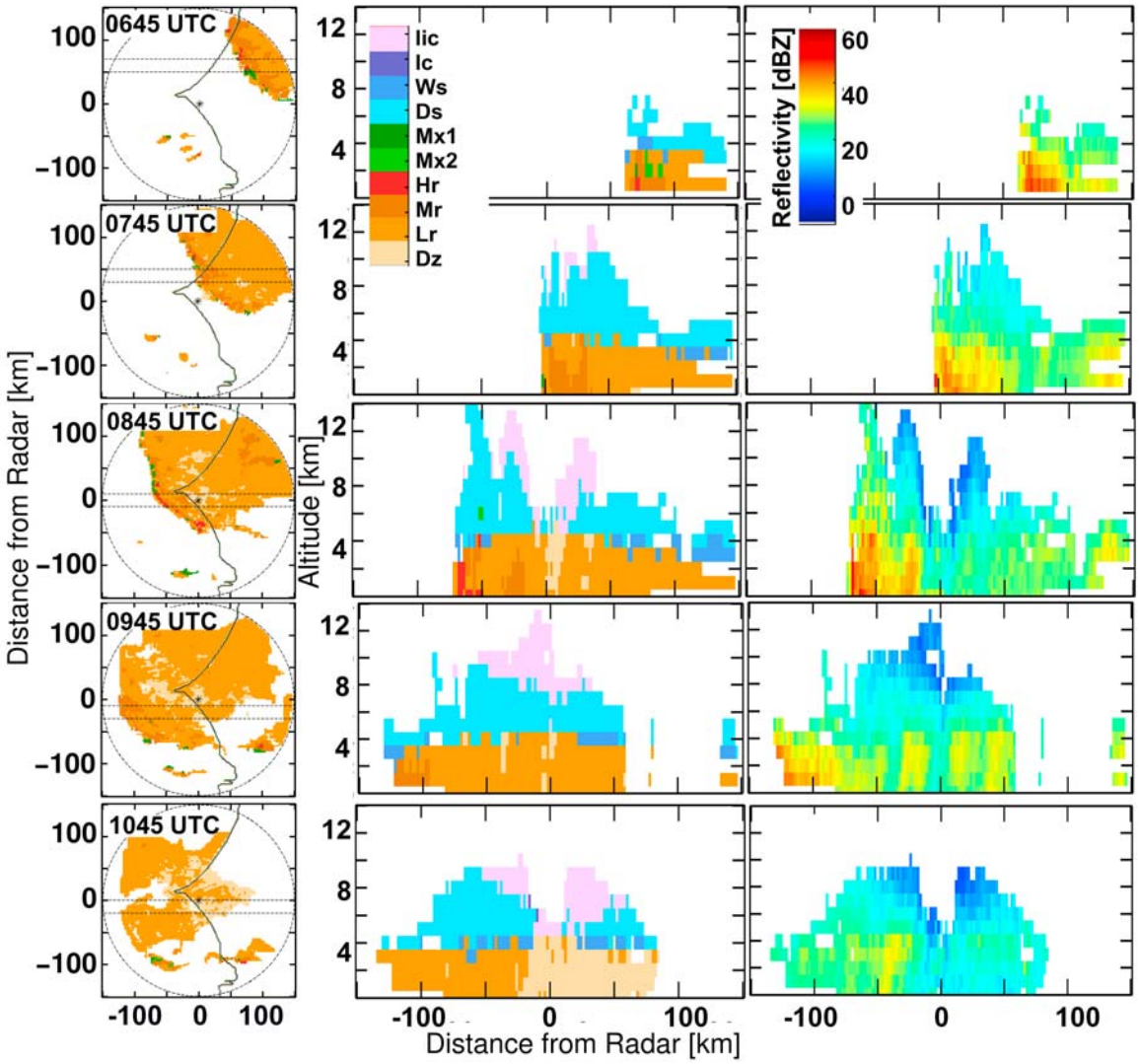

Figure 11. Vertical cross sections revealing the hourly distribution of (left) hydrometeors and (right) reflectivity values from the leading edge and through the trailing stratiform region of the 31 August 2006 MCS. The times are the same as those in Figure 3. Horizontal cross sections on the left show the distribution of hydrometeors at 2 km, as well as the east-west subsection used for the vertical cross sections (i.e., area between the two east-west transects). The hydrometeor classification identifies the most likely dominant hydrometeor in the grid among the following: ice crystals (Iic), ice crystals (Ic), wet snow (Ws), dry snow (Ds), mixed hydrometeors (Mx1, e.g., rain/graupel), mixed hydrometeors (Mx2, e.g., rain/hail), heavy rain (Hr), medium rain (Mr), light rain (Lr), and drizzle (Dz).

reflectivities (e.g., the convective region near the surface and the stratiform region within the melting layer) were statistically significant.

[37] Overall, the shapes of the reflectivity profiles within the stratiform and convective regions of the system, as well as changes in the vertical structure of the MCS as it moved to the ocean, are consistent with previous observations made using TRMM precipitation radar data [*Schumacher and Houze*, 2006; *Fuentes et al.*, 2008; *Min et al.*, 2008]. The present study provides evidence that the average patterns of reflectivity observed through these satellite measurements can be confirmed with ground-based radars as storms transition from the land to the ocean. Local observations of the boundary layer and lower troposphere indicated effective vertical mixing within the MCS, which entrained moist air masses as it propagated. Since the time scale of large convective downdrafts is on the order of 30–60 min [*Houze*, 1993], it is expected that the influence of the changing surface type (from land to ocean) can be manifested in the MCS characteristics within 1 h of moving offshore. This study supports the hypothesis that MCSs undergo a substantial transition as they propagate from land to ocean.

[38] The weakening of the system during its initial transition from the land to the ocean was likely related to its shift from a favorable (i.e., warm, moist, large wind shear, high CAPE, low CIN) to a less favorable environment. In general, tropical squall lines are known to experience lifecycle progressions over both land, where surface energy fluxes are diurnally modulated, and ocean, where fluxes remain homogeneous [e.g., *Leary and Houze*, 1979; *Trier et*

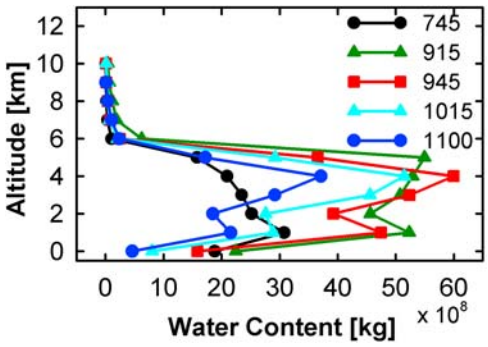

Figure 12. Total rainwater content in 1 km vertical layers in the 150 km radius range of the radar as the MCS moved from land to ocean.

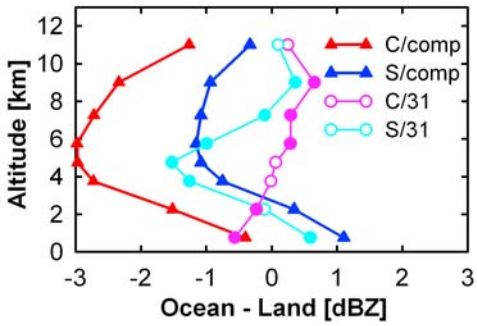

Figure 14. Differences in the profiles of mean reflectivity observed over ocean and land) in the convective (C) and stratiform (S) regions of storms. Circles represent the 31 August MCS, and triangles represent all other storms. Solid symbols indicate the vertical levels at which the differences between land and ocean samples are statistically significant ($p < 0.05$).

al., 1997]. However, it is also expected that local surface and tropospheric conditions influence the timing of intensification and dissipation of these systems [e.g., *Fuentes et al.*, 2008]. In the case presented here, observed changes in surface and tropospheric conditions at the study site (Figures 2 and 8) provide evidence that local energy and moisture were mixing into and influencing system development. This explanation is consistent with previous results that demonstrate a strong coupling among MCSs, surface-atmosphere energy exchanges [*Wang et al.*, 1996; *Tao et al.*, 1991; *Mohr et al.*, 2003; *Alonge et al.*, 2006], and heat and moisture availability in the troposphere [*LeMone and Pennell*, 1976; *Emanuel*, 1995]. Another explanation for the weakening of the system in this transition region can be related to the types of aerosols, which are known to impact cloud formation and development [e.g., *Rosenfeld*, 1999; *Khain et al.*, 2005]. Because continental air masses are more likely to have higher concentrations of terrigenous aerosols in contrast to maritime air masses laden with sea-salt aerosols, it is expected that the resulting changes in boundary layer CCN composition can influence MCS microphysics. Although it is not explicitly considered in this study, dust outbreaks can influence storm evolution in West Africa by diminishing or suppressing precipitation [*Rosenfeld*, 1999; *Min et al.*, 2008]. During spatially extensive dust outbreaks, heavy mineral dust loading can impact the expected continental-to-maritime microphysical gradients, thereby potentially obscuring or enhancing the aerosol gradient. In this way, dust outbreaks can be expected to uniquely impact the microphysics of storms as they move from the land to the ocean.

4. Summary and Conclusions

[39] The analysis of the 31 August 2006 squall line in West Africa provided evidence of the underlying impor-

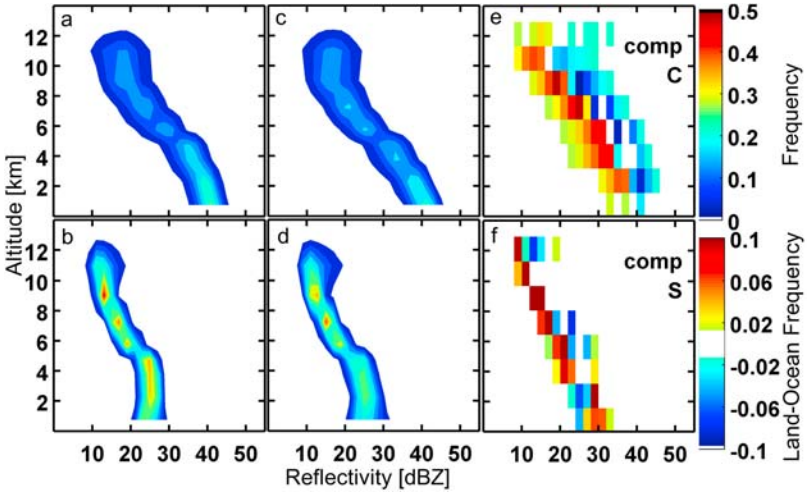

Figure 13. Composite CFADs showing the statistical properties of the vertical profiles of reflectivity (db$Z$) of seven other propagating NAMMA storms (excluding the 31 August 2006 case) in (a) the convective (C) region over land (L), (b) the stratiform (S) region over land, (c) the convective region over ocean (O), and (d) the stratiform region over ocean. (e, f) The differences in relative frequencies from land to ocean, as in Figure 10.

tance of the land-to-ocean transition and the coupling between MCSs and surface-atmosphere interactions in this transitional environment. As revealed by both radar observations and rain gauge measurements (highest reflectivity values, accumulated rainfall, and rain rates in the northeastern range of the radar), the MCS was strongest over land. The composite analysis of the 31 August MCS demonstrated a shift in intensities within both the convective and stratiform regions of the MCS as the storm moved from the continental region to the neighboring ocean. Over land, the system exhibited deep convective regions exceeding 10 km in vertical extent and producing rainfall intensities exceeding 45 mm h^{-1}. The stratiform region of the storm also produced precipitation, but less rainfall reached the surface due to low-level evaporation. Over the ocean, the convective region shifted toward lower reflectivity values, particularly in the lower atmosphere, as the storm became less organized. In the stratiform region, although it continued to develop, a similar shift in frequency isolines below the radar bright band level suggested decreasing low-level raindrop growth. The polarimetric analysis also revealed reduced rainfall yields as the MCS moved over the ocean, as well as the presence of ice in the upper regions of the cloud over the coast.

[40] Synoptic analyses indicated that antecedent thermodynamic conditions varied along the land-to-ocean transect. Specifically, specific humidity was strongest at the eastern edge of the radar range, and both total column water and SSTs decreased along an east-to-west transect. CAPE and CIN over the study site and over the Cape Verde islands also suggested that the MCS was moving to a less favorable environment during this morning event. Over land and near the coast, antecedent conditions included a history of high (>200 W m^{-2}) energy fluxes, and a warm (>30°C) and moist (specific humidity >10 g kg^{-1}) troposphere, providing a favorable environment for sustained storm propagation. Upper-air measurements at the study site confirmed that energy at the surface was mixed into the propagating system, thereby preventing it from dissipating as it reached the transition zone. The gradients, however, were likely important factors contributing to the storm weakening and disorganizing as it moved from land to ocean.

[41] Although this paper focuses on a single MCS, a composite analysis (of seven of the other propagating, spatially extensive NAMMA events) revealed similar characteristics in both convective and stratiform regions over land and ocean. In spite of the difficulty of separating the effects of the land-to-ocean transition from the natural life-cycle progression of MCSs, the consistency in results from identified major storms at different phases of their life cycles indicates that favorable coastal and maritime conditions are a prerequisite for the strengthening of organized storms capable of reaching the Cape Verde cyclogenesis region. Similarly, thermodynamic conditions over land are required to predict whether storms can intensify or dissipate prior to reaching the ocean.

[42] **Acknowledgments.** Field observations used in this study were funded by NASA for the 2006 African Monsoon Multidisciplinary Analyses project (grant MNX06AC82G). We thank Dr. Ramesh Kakar at NASA headquarters for his leadership of NAMMA. We also thank John Gerlach and his staff, who successfully deployed and operated the NPOL radar during NAMMA. The Cape Verde sounding was obtained from the NAMMA 2006 database and was provided by NASA scientist Frank Schmidlin. NCEP reanalysis data were provided by the Data Support Section of the Computational and Information Systems Laboratory at the National Center for Atmospheric Research (NCAR). The data used in the reanalysis were sourced from the U.S. Department of Commerce, the National Centers for Atmospheric Prediction, the National Weather Service, and the National Oceanic and Atmospheric Administration. NCAR, and particularly Scott Ellis, also enabled the use of the particle identification software. NCAR is supported by grants from the National Science Foundation. The ECMWF ERA-Interim data used in this study were obtained from the ECMWF data server. The University of Virginia and the Department of Environmental Sciences provided graduate student funding for M.S.D. during the time this manuscript was written. Courtney Schumacher and four anonymous reviewers provided insightful feedback to significantly improve the original manuscript.

References

Alonge, C. J., K. J. Mohr, and W.-K. Tao (2006), Numerical studies of wet versus dry soil regimes in the West African Sahel, *J. Hydrometeorol.*, *8*, 102–116, doi:10.1175/JHM559.1.

Bagayoko, F., S. Yonkeu, J. Elbers, and N. van de Giesen (2007), Energy partioning over the West African savanna: multilayer evaporation and surface conductance measurements in eastern Burkina Faso, *J. Hydrol.*, *334*, 545–559.

Berry, G. J., and C. D. Thorncroft (2005), Case study of an intense African easterly wave, *Mon. Weather Rev.*, *133*, 752–766, doi:10.1175/MWR2884.1.

Betts, A. K., J. D. Fuentes, M. Garstang, and J. H. Ball (2002), Surface diurnal cycle and boundary layer structure over Rondônia during the rainy season, *J. Geophys. Res.*, *107*(D20), 8065, doi:10.1029/2001JD000356.

Bringi, V. N., and V. Chandrasekar (2001), *Polarimetric Doppler Weather Radar*, 636 pp., Cambridge Univ. Press, New York.

Carlson, T. N. (1969), Some remarks on African disturbances and their progress over the tropical Atlantic, *Mon. Weather Rev.*, *97*, 716–726, doi:10.1175/1520-0493(1969)097<0716:SROADA>2.3.CO;2.

Cecil, D. J., and E. J. Zipser (2002), Reflectivity, ice scattering, and lightning characteristics of hurricane eyewalls and rainbands. Part II: Intercomparison of observations, *Mon. Weather Rev.*, *130*, 785–801, doi:10.1175/1520-0493(2002)130<0785:RISALC>2.0.CO;2.

da Silva, A., A. C. Young, and S. Levitus (1994), *Atlas of Surface Marine Data 1994*, vol. 1, *Algorithms and Procedures. NOAA Atlas NESDIS 6*, U.S. Dep. of Commerce, Washington, D. C.

Diedhiou, A., S. Janicot, A. Viltard, and P. de Felice (2001), Composite patterns of easterly disturbances over West Africa and the tropical Atlantic: a climatology from the 1979-95 NCEP/NCAR reanalyses, *Clim. Dyn.*, *18*, 241–253.

Diongue, A., J.-P. LaFore, J. L. Redelsperger, and R. Roca (2002), Numerical study of a Sahelian synoptic weather system: Initiation and mature stages of convection and its interactions with the large-scale dynamics, *Q. J. R. Meteorol. Soc.*, *128*, 1899–1927, doi:10.1256/003590002320603467.

Dunion, J. P., and C. S. Velden (2004), The impact of the Saharan Air Layer on Atlantic tropical cyclone activity, *Bull. Am. Meteorol. Soc.*, *85*(3), 353–365.

Eldridge, R. H. (1957), A synoptic study of West African disturbance lines, *Q. J. R. Meteorol. Soc.*, *83*, 303–314, doi:10.1002/qj.49708335704.

Emanuel, K. A. (1995), On thermally direct circulations in moist atmospheres, *J. Atmos. Sci.*, *52*, 1529–1534, doi:10.1175/1520-0469(1995)052<1529:OTDCIM>2.0.CO;2.

Emanuel, K. A. (2006), Climate and tropical cyclone activity: A new model downscaling approach, *19*, 4797–4802.

Fall, S., D. Niyogi, and F. H. M. Semazzi (2006), Analysis of mean climate conditions in Senegal (1971–1998), *Earth Interact.*, *10*(5), 1–40, doi:10.1175/EI158.1.

Feng, L., and J. Li (2006), A comparison of latent heat fluxes over global oceans for ERA and NCEP with GSSTF2, *Geophys. Res. Lett.*, *33*, L03810, doi:10.1029/2005GL024677.

Flamant, C., J.-P. Chaboureau, D. J. Parker, C. M. Taylor, J. P. Cammas, O. Bock, F. Timouk, and J. Pelon (2007), Airborne observations of the impact of a convective system on the planetary boundary layer thermodynamics and aerosol distribution in the inter-tropical discontinuity region of the West African monsoon, *Q. J. R. Meteorol. Soc.*, *133*, 1175–1189, doi:10.1002/qj.97.

Frank, N. L. (1970), Atlantic tropical systems of 1969, *Mon. Weather Rev.*, *98*, 307–314, doi:10.1175/1520-0493(1970)098<0307:ATSO>2.3.CO;2.

Frederick, K., and C. Schumacher (2007), Anvil characteristics as seen by C-POL during the Tropical Warm Pool International Cloud Experiment (TWP-ICE), *Mon. Weather Rev.*, *130*, 206–222.

Fuentes, J. D., B. Geerts, T. Dejene, P. D'Odorico, and E. Joseph (2008), Vertical attributes of precipitation systems in West Africa and adjacent Atlantic Ocean, *Theor. Appl. Climatol.*, *92*, 181–193, doi:10.1007/s00704-007-0318-0.

Futyan, J. M., and A. D. Del Genio (2007), Deep convective system evolution over Africa and the tropical Atlantic, *J. Clim.*, *20*, 5041–5060, doi:10.1175/JCLI4297.1.

Gaye, A. T., A. Viltard and P. de Félice (2005), Squall lines and rainfall over western Africa during summer 1986 and 87, *Meteorol. Atmos. Phys.*, *90*, 215–224, doi:10.1007/s00703-005-0116-0.

Geerts, B., and T. Dejene (2005), Regional and diurnal variability of the vertical structure of precipitation systems in Africa based on spaceborne radar data, *J. Clim.*, *18*, 893–916, doi:10.1175/JCLI-3316.1.

Goldenberg, S. B., C. Landsea, A. Mestas-Nunez, and W. M. Gray (2001), The recent increase in Atlantic hurricane activity: Causes and implications, *Science*, *20*, 474–479, doi:10.1126/science.1060040.

Grant, D. D., J. D. Fuentes, M. S. DeLonge, S. Chan, E. Joseph, P. Kucera, S. A. Ndiaye, and A. T. Gaye (2008), Ozone transport by mesoscale convective storms in western Senegal, *Atmos. Environ.*, *42*(30), 7104–7114, doi:10.1016/j.atmosenv.2008.05.044.

Hamilton, R. A., and J. W. Archbold (1945), Meteorology of Nigeria and adjacent Territory, *Q. J. R. Meteorol. Soc.*, *71*, 231–262, doi:10.1002/qj.49707130905.

Hirose, M., and K. Nakamura (2004), Spatiotemporal variation of the vertical gradient of rainfall rate observed by the TRMM precipitation radar, *J. Clim.*, *17*, 3378–3397, doi:10.1175/1520-0442(2004)017<3378:SVOTVG>2.0.CO;2.

Hodges, K. I., and C. D. Thorncroft (1997), Distribution and statistics of African mesoscale convective weather systems based on the ISCCP Meteosat imagery, *Mon. Weather Rev.*, *125*, 2821–2837, doi:10.1175/1520-0493(1997)125<2821:DASOAM>2.0.CO;2.

Houze, R. A. (1977), Structure and dynamics of a tropical squall-line system, *Mon. Weather Rev.*, *105*, 1540–1567, doi:10.1175/1520-0493(1977)105<1540:SADOAT>2.0.CO;2.

Houze, R. A. (1993), *Cloud Dynamics*, 539 pp., Academic, London.

Houze, R. A. (2004), Mesoscale convective systems, *Rev. Geophys.*, *42*, RG4003, doi:10.1029/2004RG000150.

Houze, R. A., and A. K. Betts (1981), Convection in GATE, *Rev. Geophys. Space Phys.*, *19*(4), 541–576, doi:10.1029/RG019i004p00541.

Hui, W. J., B. I. Cook, S. Ravi, J. D. Fuentes, and P. D'Odorico (2008), Dust-rainfall feedbacks in the West African Sahel, *Water Resour. Res.*, *44*, W05202, doi:10.1029/2008WR006885.

Kalnay, E., et al. (1996), The NCEP/NCAR 40-year reanalysis project, *Bull. Am. Meteorol. Soc.*, *77*(3), 437–471, doi:10.1175/1520-0477(1996)077<0437:TNYRP>2.0.CO;2.

Khain, A., D. Rosenfeld, and A. Pokrovsky (2005), Aerosol impact on the dynamics and microphysics of deep convective clouds, *Q. J. R. Meteorol. Soc.*, *131*, 2639–2663, doi:10.1256/qj.04.62.

Koren, I., Y. J. Kaufman, D. Rosenfeld, L. A. Remer, and Y. Rudich (2005), Aerosol invigoration and restructuring of Atlantic convective clouds, *Geophys. Res. Lett.*, *32*, L14828, doi:10.1029/2005GL023187.

Krishnamurti, T. N., S. Pattnaik, and D. Rao (2007), Mesoscale moisture initialization for monsoon and hurricane forecasts, *Mon. Weather Rev.*, *135*, 2716–2736, doi:10.1175/MWR3417.1.

Laing, A. J., and J. M. Fritsch (1993), Mesoscale convective complexes in Africa, *Mon. Weather Rev.*, *121*, 2254–2263, doi:10.1175/1520-0493(1993)121<2254:MCCIA>2.0.CO;2.

Laing, A. J., R. Carbone, V. Levizzani, and J. Tuttle (2008), The propagation and diurnal cycles of deep convection in northern tropical Africa, *Q. J. R. Meteorol. Soc.*, *134*, 93–109, doi:10.1002/qj.194.

Landsea, C. W. (2007), Counting Atlantic tropical cyclones back to 1900, *Eos Trans. AGU*, *88*(18), 197–202, doi:10.1029/2007EO180001.

Leary, C., and R. A. Houze (1979), The structure and evolution of convection in a tropical cloud cluster, *J. Atmos. Sci.*, *36*, 437–457, doi:10.1175/1520-0469(1979)036<0437:TSAEOC>2.0.CO;2.

Lebel, T., A. Diedhiou, and H. Laurent (2003), Seasonal cycle and interannual variability of the Sahelian rainfall at hydrological scales, *J. Geophys. Res.*, *108*(D8), 8389, doi:10.1029/2001JD001580.

LeMone, M. A., and W. T. Pennell (1976), The relationship of trade wind cumulus distribution to subcloud layer fluxes and structure, *Mon. Weather Rev.*, *104*, 524–539, doi:10.1175/1520-0493(1976)104<0524:TROTWC>2.0.CO;2.

Mathon, V., and H. Laurent (2001), Life cycle of Sahelian mesoscale convective cloud systems, *Q. J. R. Meteorol. Soc.*, *127*, 377–406, doi:10.1002/qj.49712757208.

Mauder, M., O. Jegede, E. Okogbue, F. Wimmerm, and T. Foken (2007), Surface energy balance measurements at a tropical site in West Africa during the transition from dry to wet season, *Theor. Appl. Climatol.*, *89*, 171–183, doi:10.1007/s00704-006-0252-6.

Min, Q.-L. Min, R. Li, B. Lin, E. Joseph, S. Wang, Y. Hu, V. Morris, and F. Chang (2008), Evidence of mineral dust altering cloud microphysics and precipitation, *Atmos. Chem. Phys. Discuss.*, *8*, 18,893–18,910.

Mohr, K., R. D. Baker, W.-K. Tao, and J. Famiglietti (2003), The sensitivity of West African convective line water budgets to land cover, *J. Hydrometeorol.*, *4*, 62–75, doi:10.1175/1525-7541(2003)004<0062:TSOWAC>2.0.CO;2.

Negri, A. J., R. F. Adler, E. J. Nelkin, and G. J. Huffman (1994), Regional rainfall climatologies derived from Special Sensor Microwave Imager (SSM/I) data, *Bull. Am. Meteorol. Soc.*, *75*(7), 1165–1182, doi:10.1175/1520-0477(1994)075<1165:RRCDFS>2.0.CO;2.

Nesbitt, S. W., and E. J. Zipser (2003), The diurnal cycle of rainfall and convective intensity according to three years of TRMM measurements, *J. Clim.*, *16*, 1456–1475.

Nicholson, S. (2000), Land surface processes and Sahel climate, *Rev. Geophys.*, *38*, 117–139, doi:10.1029/1999RG900014.

Nzeukou, A., and H. Sauvageot (2002), Distribution of rainfall parameters near the coasts of France and Senegal, *J. Appl. Meteorol.*, *41*, 69–82, doi:10.1175/1520-0450(2002)041<0069:DORPNT>2.0.CO;2.

Pandya, R., and D. Durran (1996), The influence of convectively generated thermal forcing on the mesoscale circulation around squall lines, *J. Atmos. Sci.*, *53*, 2924–2951, doi:10.1175/1520-0469(1996)053<2924:TIOCGT>2.0.CO;2.

Parker, D. J., R. R. Burton, A. Diongue-Niang, R. J. Ellis, M. Felton, C. M. Taylor, C. D. Thorncroft, P. Bessemoulin, and A. M. Tompkins (2005), The diurnal cycle of the West African monsoon circulation, *Q. J. R. Meteorol. Soc.*, *131*, 2839–2860, doi:10.1256/qj.04.52.

Rasmussen, R., and S. Rutledge (1992), Evolution of quasi-two-dimensional squall lines: Part 1. Kinematic and reflectivity structure, *J. Atmos. Sci.*, *50*, 2584–2606, doi:10.1175/1520-0469(1993)050<2584:EOQTDS>2.0.CO;2.

Rinehart, R. E. (2004), *Radar for Meteorologists*, 440 pp., Rinehart, Grand Forks, N.D.

Rogers, R. R. (1979), *A Short Course in Cloud Physics*, 2nd ed., 235 pp., Pergamon, London.

Rosenfeld, D. (1999), TRMM observed first direct evidence of smoke from forest fires inhibiting rainfall, *Geophys. Res. Lett.*, *26*, 3105–3108, doi:10.1029/1999GL006066.

Rosenfeld, D., Y. Rudich, and R. Lahav (2001), Desert dust suppressing precipitation: A possible desertification feedback loop, *Proc. Natl. Acad. Sci. USA*, *98*(11), 5975–5980, doi:10.1073/pnas.101122798.

Roux, F. (1988), The West African squall line observed on 23 June 1981 during COPT 81: Kinematics and thermodynamics, *J. Atmos. Sci.*, *45*, 406–426, doi:10.1175/1520-0469(1988)045<0406:TWASLO>2.0.CO;2.

Ryzhkov, A. V., V. Zhuravlyov, and N. Rybakova (1994), Preliminary results of X-band polarization radar studies of clouds and precipitation, *J. Atmos. Oceanic Technol.*, *11*, 132–139, doi:10.1175/1520-0426(1994)011<0132:PROXBP>2.0.CO;2.

Sall, S., and H. Sauvageot (2005), Cyclogenesis off the African coast: The case of Cindy in August 1999, *Mon. Weather Rev.*, *133*, 2803–2813, doi:10.1175/MWR3003.1.

Schumacher, C., and R. A. Houze (2003), Stratiform rain in the tropics as seen by the TRMM precipitation radar, *J. Clim.*, *16*, 1739–1756, doi:10.1175/1520-0442(2003)016<1739:SRITTA>2.0.CO;2.

Schumacher, C., and R. A. Houze (2006), Stratiform precipitation production over sub-Saharan Africa and the tropical East Atlantic as observed by TRMM, *Q. J. R. Meteorol. Soc*, *132*, 2235–2255, doi:10.1256/qj.05.121.

Smull, B. F., and R. A. Houze Jr. (1987), Rear inflow in squall lines with trailing stratiform precipitation, *Mon. Weather Rev.*, *115*, 2869–2889, doi:10.1175/1520-0493(1987)115<2869:RIISLW>2.0.CO;2.

Steiner, M., and J. A. Smith (2002), Use of three-dimensional reflectivity structure for automated detection and removal of nonprecipitating echos in radar data, *J. Atmos. Oceanic Technol.*, *19*(5), 673–686, doi:10.1175/1520-0426(2002)019<0673:UOTDRS>2.0.CO;2.

Steiner, M., R. A. Houze Jr., and S. E. Yuter (1995), Climatological characterization of three-dimensional storm structure from operational radar and rain gauge data, *J. Appl. Meteorol.*, *34*, 1978–2006, doi:10.1175/1520-0450(1995)034<1978:CCOTDS>2.0.CO;2.

Tao, W.-K., J. Simpson, and S.-T. Soong (1991), Numerical simulation of a subtropical squall line over Taiwan Strait, *Mon. Weather Rev.*, *119*, 2699–2723, doi:10.1175/1520-0493(1991)119<2699:NSOASS>2.0.CO;2.

Thorncroft, C., and K. Hodges (2001), African easterly wave variability and its relationship to Atlantic tropical cyclone activity, *J. Clim.*, *14*,

1166–1179, doi:10.1175/1520-0442(2001)014<1166:AEWVAI>2.0.CO;2.

Toracinta, E. R., D. J. Cecil, E. J. Zipser, and S. W. Nesbitt (2002), Radar, passive microwave and lightning characteristics of precipitating systems in the tropics, *Mon. Weather Rev.*, *130*, 802–824, doi:10.1175/1520-0493(2002)130<0802:RPMALC>2.0.CO;2.

Trier, S., W. Skamarock, and M. A. LeMone (1997), Structure and evolution of the 22 February 1993 TOGA COARE squall line: Organization mechanisms inferred from numerical simulation, *J. Atmos. Sci.*, *52*, 386–407, doi:10.1175/1520-0469(1997)054<0386:SAEOTF>2.0.CO;2.

Twohy, C. H., et al. (2009), Saharan dust particles nucleate droplets in eastern clouds, *Geophys. Res. Lett.*, *36*, (L01807), doi:10.1029/2008GL035846.

Vivekanandan, J., D. S. Zrnic, S. M. Ellis, R. Oye, A. V. Ryzhkov, and J. Straka (1999), Cloud microphysics retrieval using S-band dual-polarization radar measurements, *Bull. Am. Meteorol. Soc.*, *80*(2), 381–388, doi:10.1175/1520-0477(1999)080<0381:CMRUSB>2.0.CO;2.

Vömel, H., H. Selkirk, L. Miloshevich, J. Valverde, J. Valdés, E. Kyrö, R. Kivi, W. Stolz, G. Peng, and J. A. Diaz (2007), Radiation dry bias of the Vaisala RS92 humidity sensor, *J. Atmos. Oceanic Technol.*, *24*(6), 953–963, doi:10.1175/JTECH2019.1.

Wang, Y., W.-K. Tao, and J. Simpson (1996), The impact of ocean surface fluxes on a TOGA COARE convective system, *Mon. Weather Rev.*, *124*, 2753–2763, doi:10.1175/1520-0493(1996)124<2753:TIOOSF>2.0.CO;2.

Webster, P. J., G. J. Holland, J. A. Curry, and H. R. Chang (2005), Changes in tropical cyclone number, duration, and intensity in a warming environment, *Science*, *309*(5742), 1844–1846, doi:10.1126/science.1116448.

White, A. B., C. W. Fairall, and J. B. Snider (1995), Surface-based remote sensing of marine boundary-layer cloud properties, *J. Atmos. Sci.*, *52*(16), 2827–2838, doi:10.1175/1520-0469(1995)052<2827:SBRSOM>2.0.CO;2.

Yoneyama, M., M. Fujita, N. Sato, M. Fujiwara, Y. Inai, and F. Hasebe (2008), Correction for radiation dry bias found in RS92 radiosonde data during the MISMO field experiment, *SOLA*, *4*, 13–16, doi:10.2151/sola.2008-004.

Yuter, S. E., and R. A. Houze (1995), Three-dimensional kinematic and microphysical evolution of Florida cumulonimbus: Part II. Frequency distributions of vertical velocity, reflectivity, and differential reflectivity, *Mon. Weather Rev.*, *123*, 1941–1963, doi:10.1175/1520-0493(1995)123<1941:TDKAME>2.0.CO;2.

Zipser, E. J. (1969), The role of organized unsaturated convective downdrafts in the structure and rapid decay of an equatorial disturbance, *J. Appl. Meteorol.*, *8*, 799–814, doi:10.1175/1520-0450(1969)008<0799:TROOUC>2.0.CO;2.

Zipser, E. J., and K. R. Lutz (1994), The vertical profile of radar reflectivity of convective cells: A strong indicator of storm intensity and lightening probability? *Mon. Weather Rev.*, *122*, 1751–1759, doi:10.1175/1520-0493(1994)122<1751:TVPORR>2.0.CO;2.

Zipser, E. J., D. J. Cecil, C. Liu, S. W. Nesbitt, and D. P. Yorty (2006), Where are the most intense thunderstorms on Earth? *Bull. Am. Meteorol. Soc.*, *87*(8), 1057–1071, doi:10.1175/BAMS-87-8-1057.

S. Chan, J. D. Fuentes, and M. S. DeLonge (corresponding author), Department of Environmental Science, University of Virginia, 291 McCormick Rd., Charlottesville, VA 22904, USA. (msd8y@virginia.edu)

B. Daouda and A. T. Gaye, Laboratoire de Physique de l'Atmosphère et de l'Océan-Siméon Fongang, Ecole Supérieure Polytechnique, University Cheikh Anta Diop, 5085 Dakar, Senegal.

E. Joseph, Department of Physics and Astronomy, Howard University, 2355 6th St. NW, Washington, DC 20059, USA.

P. A. Kucera, Research Applications Laboratory, National Center for Atmospheric Research, PO Box 3000, Boulder, CO 80307, USA.